Waste Management 140 (2022) 110–120

Contents lists available at ScienceDirect

Waste Management

journal homepage: www.elsevier.com/locate/wasman

Closing the loop: Valorizing pyrolyzed waste tyre residue into functional carbon materials, SiO_2 with exceptionally high silanol groups, and Zn salt

Javier A. Jimenez Forero [a,d], Athukoralalage Don K. Deshan [a], Jorge Beltramini [a,c], John Bartley [b], Ekaterina Estrounina [e], William O.S. Doherty [a,*]

[a] Centre for Agriculture and the Bioeconomy, Queensland University of Technology, Brisbane 4000, Australia
[b] School of Chemistry and Physics, Queensland University of Technology, Brisbane 4000, Australia
[c] IROAST, Department of Chemistry, Faculty of Advanced Science and Technology, Kumamoto University, Kumamoto, Japan
[d] Faculty of Science and Natural Resources, University of Los Llanos, Villavicencio 500017, Colombia
[e] Centre for Advanced Imaging, The University of Queensland, Brisbane 4072, Australia

ARTICLE INFO

Keywords:
Waste management
Porous carbon
Pyrolysis
Mineral recovery
Functionalization

ABSTRACT

This study aims to identify suitable processing conditions for converting pyrolytic solid residue from off-the-road tyres (OTR) to improve carbon materials properties that can be used in multiple applications and the recovery of minerals from OTR. Pyrolysis of OTR at 800 °C and a heating rate 2 °C.min^{-1} gave a carbon material with the highest surface area, most defective carbon structures, and the highest micro-porosity. This operating condition was used to compare the conventional three-step carbonization approach, which involves a demineralization stage that produces high volumes of toxic wastewater, with a two-step approach that bypasses this stage. Analysis of the carbon structures showed that the quality of the carbon material from the two-step approach is similar to the three-step approach. This two-step approach resulted in a solid and a liquid phase, in which ~ 93.4% of Zn was selectively fractionated to the liquid phase. The wastewater from the acid wash of the carbonized OTR was neutralized to recover the SiO_2, of which 55.5% was reactive SiO_2. The SiO_2 was found to have an exceptionally high cross-linking ratio of 5.94, achievable only when SiO_2 is reacted with silane groups. The study demonstrated that the engineered carbon material from OTR has a H_2 uptake of 1.03 wt% at 77 K and 1.2 bar, and the sulfonated counterpart was an effective catalyst (64% conversion) for the Aldol condensation of levunilic acid to two dimer products [tetrahydro-2- methyl-5,γ-dioxo-2-furanpentanoic acid (TMDFA) and 3-(2-methyl-5-oxo-tetrahydrofuran-2-yl)-4-oxopentanoic acid (MOTOA)] that are precursors for fuels and chemicals.

1. Introduction

The exponential buildup of tyres used for industrial and domestic purposes account to around 1.5 billion units/year worldwide, with 17 million waste tyre tons/year accumulated in landfills and stockpiles, causing severe environmental concerns (Wang et al., 2019). In Australia alone, 465,000 tonnes of tyres reached their end of life during 2018–2019. Among them, 44% are managed in Australia, where just 14% are reused and the rest, mainly consisting of off-the-road tyres (OTR), are disposed on-site or in landfills (Randell et al., 2020).

In accordance with new UN's 2030 environmental policies, the Australian Government focuses on implementing environmentally friendly processes to manage all forms of waste during its life cycle to minimize toxic emissions, which affect public health and the environment (Australian Government, 2018). For this purpose, circular processes need to be established to ensure productive use of goods as much as possible, progressively reintegrating, reusing, and designing sustainable waste utilization systems.

Abbreviations: APS, average particle size; BET, Brunauer-Emmett-Teller; CPMAS, cross-polarization magic angle spinning; EDS, energy dispersive spectroscopy; EtOH, ethanol; FFT, Fast Fourier transform images; ICP-OES, Inductively coupled plasma atomic emission spectroscopy; IFFT, Inverse fast Fourier transform images; LA, levulinic acid; LDCC, less-developed crystalline carbon; NLDFT, non-local density functional theory; MOTOA, 3-(2-methyl-5-oxo- tetrahydrofuran-2-yl)-4-oxopentanoic acid; MDCC, more-developed crystalline carbon; NMR, nuclear magnetic resonance; OTR, Off the road tires; SEM, scanning electron microscope; SP-hpdec, Single pulse high power decoupling; SSNMR, Solid-state NMR; TBP, Tributyl phosphate; TMDFA, tetrahydro-2- methyl-5,γ-dioxo-2-furanpentanoic acid; XPS, X-ray photoelectron spectra; XRD, X-ray powder diffraction; XRF, X-ray fluorescence.

* Corresponding author.
E-mail address: w.doherty@qut.edu.au (W.O.S. Doherty).

https://doi.org/10.1016/j.wasman.2022.01.018
Received 14 October 2021; Received in revised form 20 December 2021; Accepted 16 January 2022
Available online 22 January 2022
0956-053X/© 2022 Elsevier Ltd. All rights reserved.

Among thermal decomposition of tyres, pyrolysis has been proposed as a promising technology to recover energy and fuel because of its low emissions and energy savings, producing 36–38 wt% oil, 12–16 wt% pyro-gas, and 46–50 wt% of solid residue (Antoniou and Zabaniotou, 2018). The profitability of pyrolysis technology in processing OTR relies largely on finding applications for its solid residue, such as adsorbents (Danmaliki and Saleh, 2017, 2016; Saleh and Danmaliki, 2016), additives for rubber goods (Cardona et al., 2018), and as a feedstock for activated carbon production (Martínez et al., 2019). The main issue with OTR solid residue upgrading is its lower surface area and higher mineral content (10–20 wt%) compared to commercial carbon blacks and activated carbons (Antoniou and Zabaniotou, 2018). For this reason, increasing research relating to its demineralization and surface area improvements have been conducted either during single or both pre, post-activation by chemical treatments in liquid–solid systems with alkali and acid solutions (Iraola et al., 2018). It was found that an improvement in the quality of carbons could be obtained if acid treatment is first used for demineralization before chemical treatment and carbonization. However, this initial treatment requires a large volume of water to wash the carbon residue to remove dissolved salts and acid before carbonization. The disposal of this wastewater to the environment is hazardous because of the presence of Zinc salts and other impurities originating from OTR. The proportions of the inorganic salts removed from OTR vary and depend on the type and concentration of the demineralizing agent used. It has been reported that concentrated HCl and H_2SO_4 can remove up to 59% and 41% of inorganics, respectively (Shah et al., 2006), while other research groups reported values from 15%->90% (Henry, 2015; Manocha et al., 2013; Pilusa and Muzenda, 2013). The same variance was found when using pure HCl or NaOH (Iraola et al., 2018) or in different combinations such as HCl/HNO_3 (Akyildiz et al., 2010) and HCl/HF (Zhang et al., 2018). After the demineralization step, the chemical activation process (*e.g.*, KOH and K_2CO_3) at high temperatures (>700 °C) is carried out (Mwafy, 2020). The conventional method used to produce carbons for commercial application from OTR involves three steps: (i) acid pretreatment or demineralization, (ii) chemical activation (*e.g.*, KOH), and carbonization/pyrolysis, and (iii) acid wash. Unfortunately, this process produces hazardous impurities which pollute the environment, and to date there is no report on the effective recovery of these mineral impurities. In addition, no study has been carried out to engineer OTR to a carbon material suitable to be used as catalyst or energy storage.

To address these gaps, this project evaluated different processing conditions for OTR in order to produce an engineered carbon material with multifacet applications and identify a process to manage the hazardous waste impurities generated in the process. To tackle the toxic waste issue associated with the conventional three-step approach, a two-step approach that eliminates the acid demineralization step was proposed. The inorganics Zn, Si, and Fe from the aqueous solution after acid wash of the carbonized material obtained by the two-step approach were recovered, significantly reducing the ecosystem's pollution and, at the same time, potentially improving the economics of OTR processing to carbon products. The Zn salts could potentially be upgraded to high-value Zn metal. The neutralization step we adopted to recover the inorganics in the acid wash solution was to ensure that reactive silanol groups were preserved in the SiO_2 matrix so that it can be reused in tyre manufacture, adsorption applications, or for lithium-ion batteries because of its high cross-linking density ratio (Entwistle et al., 2018; Jamiu and Ali, 2019). This study also demonstrated the potential applications of the engineered carbon materials for H_2 storage and as a catalyst for the catalytic Aldol condensation of levulinic acid to lactone acids, which are valuable feedstocks for producing fuels and chemicals.

2. Experimental section

2.1. Material and chemicals

Pyrolyzed solid residue derived from the off-the-road tyres (OTR) was obtained from Green Distillation Technologies, NSW–Australia. KOH, HCl, K_2CO_3, H_2SO_4 (98 wt%), Tributyl phosphate (TBP), and ethanol (EtOH) were reagent grade and purchased from Merck (Kilsyth, VIC Australia).

2.2. Material preparation

OTR (50 g) was dried for 24 h at 45 °C under vacuum. It was submerged in liquid nitrogen and grounded for 10 min using a ball-milling machine (TissueLyserII QIAGEN®). The resulting powder material was sieved (sieve number 120), and 47.5 g of the fraction < 125 μm was collected and stored in closed containers at room temperature.

2.3. Demineralization and carbonization processes

The carbonization condition selected for the detailed study of OTR were at 600, 700, and 800 °C, and three different heating rates of 2, 5, and 10 °C.min^{-1}. The samples were held at the final temperature for 1 h using a tube furnace (NBD-O1200-50IT) with a flowing stream of nitrogen (200 mL.min^{-1}). Higher temperatures were not selected because the goal was to obtain conducting carbons (rather than activated carbon) and not reduce the carbon yield significantly. Also, lower heating rates were not considered because this will increase energy consumption and will only give minimum benefits (Wang et al., 2020).

Three different methods (duplicate runs) were used to activate and carbonize OTR. The carbonization condition of 2 °C .min^{-1} to 800 °C and holding at that temperature for 1 h was selected from the initial studies.

2.3.1. Ethanol (EtOH) and chemical activation

OTREtK1:2 was prepared by mixing 1 g OTR + 150 mL EtOH + 2 g KOH and stirred at 40 °C for 1 h, and then the mixture was dried at 60 °C to constant weight followed by carbonization. OTRNEtK1:2 was prepared by mixing 1 g OTR + 200 mL HCl (1 M) and boiled for 3 h, filtered and dried to constant weight at 60 °C. Following this, 200 mL of 15% NaOH was added and the mixture was boiled for 4 h, filtered and dried to constant weight at 60 °C. To this solid, 10 mL EtOH + 2 g KOH was added; the mixture was stirred at 40 °C for 1 h, then dried at 60 °C to constant weight followed by carbonization.

2.3.2. KOH/alkali activation (two-step approach)

OTRK1:2 was prepared by grinding in a porcelain mortar 1 g OTR + 2 g KOH solid. OTRK1:4 was prepared by grinding a porcelain mortar 1 g OTR + 4 g KOH. OTRN1:2 was prepared by grinding in a porcelain mortar 1 g OTR + 2 g NaOH followed by carbonization.

OTRKC1:2 was prepared by grinding in a porcelain mortar 1 g OTR + 2 g K_2CO_3.

2.3.3. HCl/KOH activation (three-step approach)

OTRHK1:2 was prepared by mixing 1 g OTR + 200 mL HCl (1 M) boiled for 3 h, filtered and the residue dried to constant weight at 60 °C. The residue was then mixed with 2 g KOH, and the mixture ground in a porcelain mortar. The mixture was then carbonized. OTRHK1:4 was prepared by mixing 1 g OTR + 200 mL HCl (1 M) boiled for 3 h, filtered and the residue dried to constant weight at 60 °C. The residue was mixed with 4 g KOH and the mixture ground in a porcelain mortar. The mixture was then carbonized.

After activation and carbonization, all the samples were washed with 20 mL of 2 M HCl per g of carbon under constant stirring (no<2 h). The produced carbons were filtered and washed with Milli Q water until neutral pH. The samples were recovered and dried in a vacuum oven at 45 °C for 24 h.

2.4. Carbon characterization

The elemental (CHNSO) analysis was performed using a Flash EA 1112 Organic Analyzer (Thermo Scientific, USA). The other elements were acquired by X-ray fluorescence (XRF) analysis in an ED-XRF spectrometer (Ametek SPECTRO XEPOS), a minimum of 300 s pulse collection time per target protocol was utilized. Resultant spectra were interpreted using a training set that includes SARM-20 and GSS-1. Sodium was excluded from the analysis routine due to poor fluorescent yield and high attenuation factor of fluorescent X-rays by the sample and detector windows (infinite thickness of Na Kα in graphite ≈ 12 μm).

The BET surface area (S_{BET}), total pore volume (V_T), and pore size distribution of the samples were examined using N_2 adsorption at −196 °C on a surface area analyzer (Micromeritics 3-flex, USA). The material was degassed under vacuum at 250 °C for at least 12 h before the measurement. The S_{BET} of the prepared carbon was estimated by BET (Brunauer–Emmett–Teller) method. The pore volume (V_T), pore size distribution, and average particle size (APS) of the prepared carbon were estimated by density functional theory (N_2 at 87 K-Carbon: slit, pore, NLDFT), micro, meso, and macro surface area and porosity volume were calculated using the cumulative surface area and volume in the vapour pressure region $P/P_o = 0.01–0.99$ (Kupgan et al., 2017). The data were analyzed using the software 3Flex version 4.05, Micromeritics®.

Surface morphology and structure were evaluated using a scanning electron microscope, SEM (Tescan Mira3, CZE), equipped with an energy dispersive spectroscopy (EDS). Transmission electron microscopy (TEM) was performed using a TEM (Jeol 1400, USA) operated at 200 kV. Raman vibrational spectroscopy was used to assess the disordered structure and existence of graphitic carbon at 532 nm (inViaTM – Renishaw, UK) at Raman shifts between 800 and 3500 cm^{-1}. X-ray photoelectron spectroscopy (XPS) was conducted using a Kratos Axis Supra (Kratos Analytical, LLC) equipped with an Al anode, base pressure of 1×10^{-7} Torr, and conducting a fixed analyzer transmission (FAT). The x-ray source power was 225 Watts, the pass energy during survey spectra was 160 eV using a step size of 1 eV and a dwell time of 200 ms. High-resolution spectra were acquired with a step size of 0.05 eV and a dwell time of 1.6 s per channel at the same power. Spectra were processed using CasaXPS version 2.3.22PR1.0 and corrected in binding energy by rigidly shifting each dataset to put the C1s intensity maximum at 284.8 eV.

The X-ray powder diffraction (XRD) patterns were measured using Bruker D8 Advance Diffractometer under CoKα radiation (λ = 1.7902 Å). A variable divergence alit illuminates a constant 10 mm sample length. An automatic knife edge above sample to block air-scattering background. A 2.5° Soller slit was used on both the primary and secondary sides to control axial divergence. A LynxEye XE-T detector was operated in 1D high energy resolution mode. Each sample was measured from 2 to 90° at 0.015° 2θ step size in 1 h. The standard external method was employed to establish absolute phase abundances by simultaneously acquiring a pure corundum pattern as the samples get through similar scan conditions. Phase classification was accomplished employing the ICDD PDF4 + database in EVA (V5, Bruker). As applied in TOPAS (V6, Bruker), the Rietveld method was utilized for refinement and quantitative phase analysis. Peak shapes were modelled via a measured instrument function determined from SRM 660a (NIST, LaB6).

From XRD results, lattice parameters such as the interlayer space (d_{002}), the heigh (L_a), the diameter (L_c) of crystallites sites and the average number of aromatic layers (N_{ave}) in less-developed crystalline carbon (LDCC) and more-developed crystalline carbon (MDCC) were estimated by applying the Bragg's (Eq. (1)), and Scherrer derived equations (Eqs. (2)–(4)) (Meng et al., 2019).

$$d_{002} = \frac{\lambda}{2sin\theta_{002}} \tag{1}$$

$$L_c = \frac{S\lambda}{\beta_{002}cos\theta_{002}} \tag{2}$$

$$L_a = \frac{S\lambda}{\beta_{100}cos\theta_{100}} \tag{3}$$

$$N_{ave} = \frac{L_c}{d_{002}} + 1 \tag{4}$$

Where, S: shape parameter −0.89(L_c) and 1.84(L_a); λ: Co-X-ray wavelength (1.78897 Å); β: full width at half-maximum FWHM (in degrees) of (1 0 0) and (0 0 2) planes, θ: diffraction angle in degrees of (1 0 0) and (0 0 2) planes.

2.5. Recovery of inorganics from the acid wash solution

The process to recover minerals is described in Fig. A1. The acid wash solution was obtained when 20 mL of 2 M HCl per g of treated carbon was added. 50 mL of this solution was stirred at 200 rpm followed by the slow addition of KOH 50% (w/v %) solution to raise the pH of the solution to 6. This was then followed by the slow addition of 0.1 M KOH to pH 7. The solution was mechanically mixed with 50 mL of TBP for 30 min for Zn and Fe salts recovery (Montes and Hill, 2018). The two phases formed were divided in a separating funnel; the precipitate in the aqueous phase was separated by centrifugation (3900 rpm, 10 min) and washed with Milli Q water for SiO_2 recovery. A rotary evaporator concentrated the K-rich liquid. The analysis of the acid wash solution and the aqueous phase after TBP treatment was performed using an inductively coupled plasma optical emission spectrometry (ICP-OES) on a Perkin Elmer ICP-OES 8300DV (Waltham, MA, USA) fitted with an ESI SC-4DX autosampler and PrepFAST 2 sample handling unit for online internal standardization and auto dilution of calibration standards (high purity standards, Charleston, USA). The recovered SiO_2 was analyzed by SEM-EDS, FTIR-ATR, and solid-state NMR spectroscopy.

Solid-state NMR (SSNMR) experiment of the SiO_2 was performed on a Bruker Avance III spectrometer with a 300 MHz magnet equipped with a 4 mm double air bearing, magic angle spinning probe. The powdered samples were placed in zirconia rotor with a Kel-F cap and rotated at 5 kHz. ^{29}Si spectra were recorded with cross-polarisation magic angle spinning (CPMAS, time was 5 ms, decoupling power 100 kHz) and single pulse high power decoupling (SP-hpdec, repetition delay was 30 s for complete relaxation.) pulse sequences. The CPMAS data was used to confirm peak positions. Relative peak areas were then calculated from SP-hpdec spectrum.

3. Results and discussion

3.1. Effect of carbonization conditions on carbon structure development

N_2 adsorption–desorption isotherms of the materials prepared at various carbonization temperatures and heating rates are shown in Fig. 1(i, ii, iii). According to the IUPAC classification, the isotherms belong to a predominantly type II behaviour (Brunauer et al., 1938). A pseudotype II behaviour with a narrow hysteresis loop of type H3 was observed above 0.8 relative partial pressure for all samples, confirming the presence of slit-shaped pores with low pore curvatures and non-firmness aggregate arrangement (Sing and Williams, 2004). The early part of the isotherms shows some nitrogen uptake at low relative pressures, corresponding to micropores adsorption. Total nitrogen adsorption decreases with increasing activation temperature from 600 to 700 °C. However, it increases again from 700 to 800 °C, but only under slow heating rates. The surface area (S_{BET}) data follow a similar trend (Fig. 1(iv-a), Table A1), as a result of the increased microporosity, which accounts for 34.23% of the S_{BET}, and the presence of interparticle mesoporosity, associated with smaller particle size (36.58 nm) under these

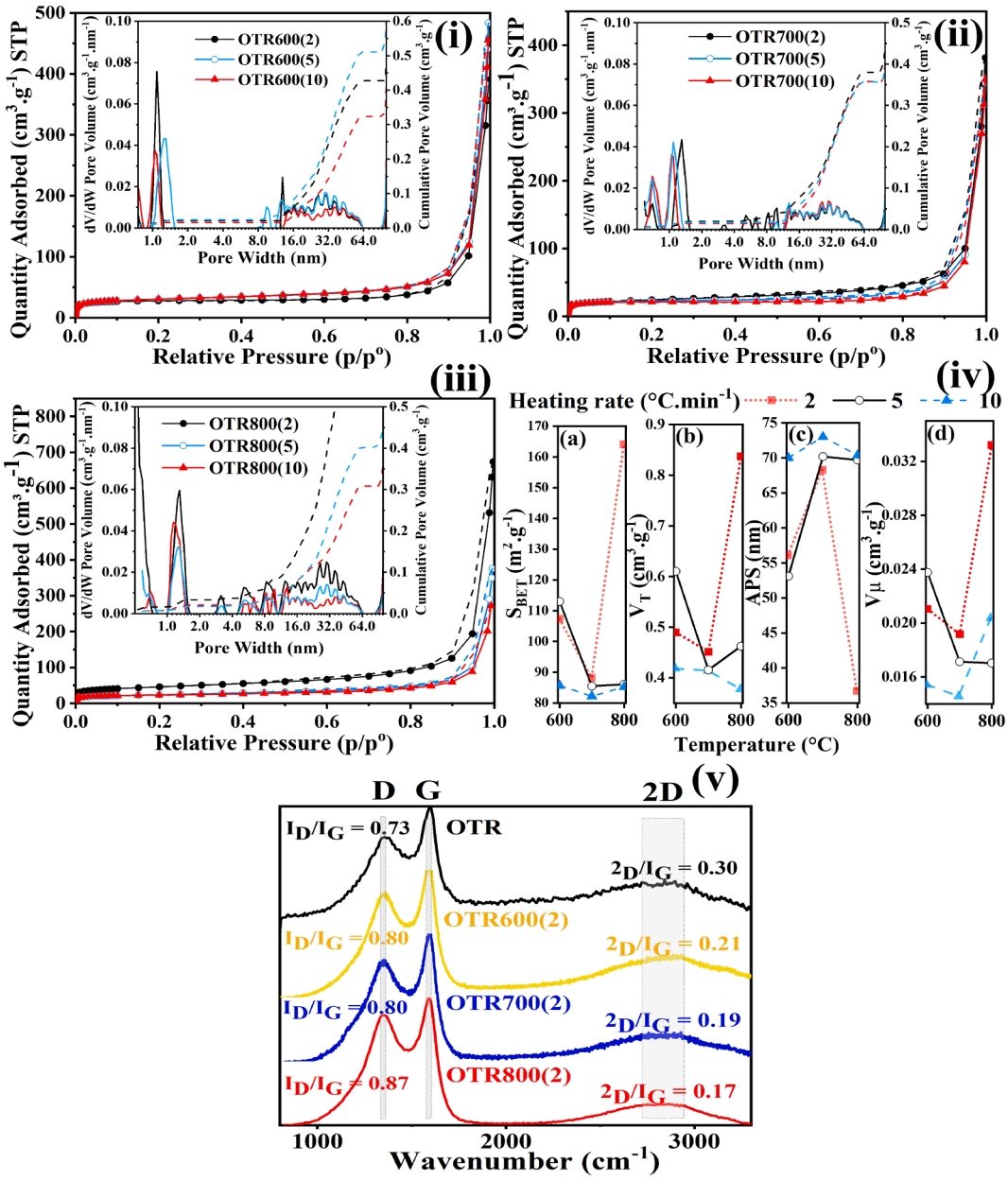

Fig. 1. N_2 adsorption–desorption isotherms at 77 K and their respective pore size distribution via NLDFT for the carbons processed at different carbonization conditions 600 °C (i), 700 °C (ii) and 800 °C (iii). Interactive effect of temperature and heating rate (iv) on S_{BET} (a), V_T (b), APS (c) and (d) Vμ. Raman spectra of OTR and carbons produced at 2 °C.min^{-1} (v).

conditions (Fig. 1(iv-c)). At 600 °C it is likely that there is enough energy to generate interparticle structures independent of the heating rate, but reaching 700 °C a more denser packing of the carbon arrangement was detected, affecting contact with the internal structures. Nevertheless, at 800 °C and slow heating rate, an opening of the particle structure was observed, in contrast to using higher heating rates where the char particles can melt, flattening the carbon structure. This behavior was confirmed by the SEM images where reducing the heating rate reduced the particle size, helping the nonconglomeration of numerous granules aggregated by the pseudo- spherical particles (Fig. A2).

The total pore volume (V_T) varied between 0.38 and 0.84 cm^3.g^{-1}, following a similar trend as S_{BET} and Vμ as a function of the temperature follows a similar trend as S_{BET} and Vμ. The total (V_T), micro (V_μ), meso, and macropore volume is highest at 800 °C and a heating rate of 2 °C.min^{-1} (Fig. 1(iv-a)). This observed trend can be associated with the development of particle bed void with interparticle channel openings due to the formation of interparticle mesoporous channels which are typical of carbon black materials with large particle sizes (Macías García et al., 2020). Regarding the interactive effect of temperature and heating rate on the average particle size (APS), raising the temperature from 600 to 700 °C increased the particles growth. However, a significant decrease was observed at 800 °C and 2 °C.min^{-1} (Fig. 1(iv-c)), as slow heating rates could affect the oxidation of internal carbon walls, and as a result, increase of the internal surface area and the V_T. The drop in the average particle size at the higher temperature is unknown but could be related to the rearrangement of the carbon structures under these conditions. Although these resulting materials from our studies have low surface areas but reasonable microporosity may find applications as chemical filters or supercapacitors electrodes (Gupta et al., 2015). The Raman spectra (Fig. 1-v and Fig. A3) for the carbonized samples show the presence of G-band (1589 cm^{-1}) characteristics of a graphitic structure ascribed to the in-plane vibration of sp^2 carbon atoms in

graphene layers. On the other hand, the D-band (1353 cm^{-1}) is attributed to sp^3 carbons of the amorphous structure typical of carbon materials (Sanchez Olmos et al., 2017). The average I_D/I_G compared at the same heating rate of 2 °C.min^{-1} and 800 °C is 0.87 vs 0.80 at 700 °C and 600 °C respectively (Fig. 1-v), suggesting the presence of a more defective carbon structure obtained at higher temperatures, correlating with an increased aromatic structure formation, where the crystallization of sp^2 amorphous carbon creates graphitic networks as the temperature is raised (Zhang et al., 2018). Results also show a decreased pattern in the formation of layered structures ($2_D/I_G$) when the temperature increases, possibly ascribable to reduced interactions between the carbon layers and the functional groups (Hao et al., 2010). Based on the physical properties for all tested carbons, the carbon structure obtained at 800 °C at 2 °C.min^{-1} heating rate was then selected as the more suitable to assess the various chemical treatment methods during the carbonization of OTR.

3.2. Effect of chemical treatment on the chemical composition of the carbons

Table 1 shows the CHNOS analysis for OTR, carbonized OTR, and the chemically treated and carbonized OTR. The carbon contents are higher in the chemically treated samples compared to no chemical treatment as the inorganic salts were removed during the process. Mineral removal with subsequent increase in the surface area during chemical treatments increased the adsorption of oxygen species on the surface of the carbon because of the formation of metal oxides. The conventional three-step process reduced/eliminated sulfur, reduced hydrogen and oxygen contents, and has lower H/C and O/C than the two-step process. So, the demineralization process with HCl does remove some sulfur species before the carbonization process. The wet impregnation with EtOH (Table 1, entries 3 and 4) increased both carbon and oxygen contents compared when only mechanical mixing was used (Table 1, entry 6). Presumably, residual EtOH assisted the burn-off of the material, providing additional oxygen species that spills on the surface of the carbon material enhanced by the presence of residual metal impurities.

From the XRF analysis (Table 1), it can be seen that the combined chemical treatment and carbonization process considerably reduced the total mineral content by a maximum of 64.68%. Of significance though, is the almost complete removal of Zn after chemical treatments. The amount of Si was also considerably reduced, though the addition of NaOH during the activation process was the most effective for Si reduction. This was expected as Si is readily soluble in NaOH to form soluble silicate salts. As previously stated, the amount of sulphur was also significantly reduced, particularly with the three-step approach. Overall, the two-step approach is similarly effective as the three-step approach to remove inorganics from OTR. XPS analysis (Table A2, Fig. A4) confirmed that the highest carbon content material was obtained with OTRK1:4, the sample derived by the two-step approach (Table 1, entry 6), where no Zn, S, or Si was detected on the surface (Fig. A5(b)). In comparison, OTRHK1:4, obtained by the three-step approach, contains Si on the surface (Table 1, entry 8). It is plausible that the HCl demineralization step dehydrated the Si species making them more difficult to be removed by alkali in the subsequent activation and carbonization steps. As explained in a previous study, the removal of Si present in the scale deposited in sugar mill evaporators by HCl treatment results in the polymerization of SiO_2 species forming Q_3 and Q_4 SiO_2 structures that were more difficult to remove by subsequent caustic soda treatment (Phakam et al., 2017). The use of K_2CO_3 (Table 1, entry 10), although at a lower dosage of 1:2 was equally effective in removing Si, Zn, and S, with a lower carbon content on the final material. During the sample impregnation using lower dosages of KOH (Table 1, entries 3 and 4), it was found reduced O1s contents compared to the grinding process (Table 1, entry 5), again likely due to increased burn-off of residual ethanol.

The XRD patterns (Fig. A5(a)) confirm both the XRF and XPS data showing that the two-step process is a suitable treatment method for OTR as it effectively removes inorganic mineral impurities from OTR. Therefore, the demineralization step can be eliminated, reducing disposal and management costs associated with upgrading OTR to valuable products for a cleaner production process.

3.3. Physical and structural properties of carbons

From the N_2 isotherms (Fig. 3(a), (b), A6) it was also observed that the S_{BET} of the KOH-derived carbons is higher than those derived when using NaOH and K_2CO_3 (Table 2, entries 7 and 8). This can be explained as K^+ ions released from KOH at ≥ 600 °C are more efficient in creating microporous structures which increase the internal surface area of carbons than Na^+ ions (Linares Solano et al., 2012). The K can be formed

Table 1
Inorganic constituents by XRF and elemental analysis of OTR and carbonized OTR obtained by heating at 2 °C.min^{-1} to 800 °C and holding time of 1 h under nitrogen atmosphere.

		Sample									
		(1)	(2)	(3)	(4)	(5)	(6)	(7)	(8)	(9)	(10)
		OTR	OTR800 (2)	OTREtK1:2	OTRNEtK1:2	OTRK1:2	OTRK1:4	OTRHK1:2	OTRHK1:4	OTRN1:2	OTRKC1:2
XRF analysis	SiO_2 (%)	6.11	5.88	4.35	1.90	2.98	3.71	3.31	2.17	1.38	2.95
	SO_3 (%)	7.77	5.86	1.88	1.20	1.80	0.90	2.54	2.88	3.63	1.92
	Fe_2O_3 (%)	1.28	0.71	0.56	0.18	0.68	0.23	1.10	0.75	0.97	1.06
	ZnO (%)	6.06	4.34	0.10	0.01	0.05	0.01	0.06	0.04	0.01	0.05
	K_2O (%)	0.19	0.09	3.93	4.08	2.94	0.92	1.84	1.00	0.45	5.17
	Al_2O_3 (%)	0.63	–	0.52	0.41	0.42	0.21	0.38	0.50	0.42	0.54
	Others (%)	2.59	1.60	1.47	1.05	1.77	1.21	1.66	2.02	1.82	1.68
	Total (%)	24.63	18.48	12.81	8.83	10.64	9.08	10.89	9.35	8.70	13.37
	Minerals removed (%)	0.00	24.97	47.99	64.15	56.80	63.13	55.79	62.04	64.68	45.72
Elemental analysis	C (wt.%)	74.40	73.40	78.60	78.48	75.37	81.11	78.40	87.39	75.62	77.41
	N (wt.%)	0.10	0.30	0.30	0.27	0.17	0.07	0.00	0.07	0.41	0.30
	H (wt.%)	1.30	0.60	0.60	0.66	0.92	1.32	1.00	0.94	0.75	0.70
	S (wt.%)	0.30	0.30	0.40	0.17	0.33	0.62	0.40	0.00	0.04	0.00
	O (wt.%)	3.80	1.50	8.20	8.32	7.09	5.81	5.50	4.30	8.50	7.30
	Molar ratio H/C	0.22	0.10	0.10	0.10	0.15	0.20	0.16	0.13	0.12	0.11
	O/C	0.04	0.02	0.08	0.08	0.07	0.05	0.05	0.04	0.08	0.07

Error in duplicate results for C, H, N, S, O (<0.2%), and for XRF (<0.3%).

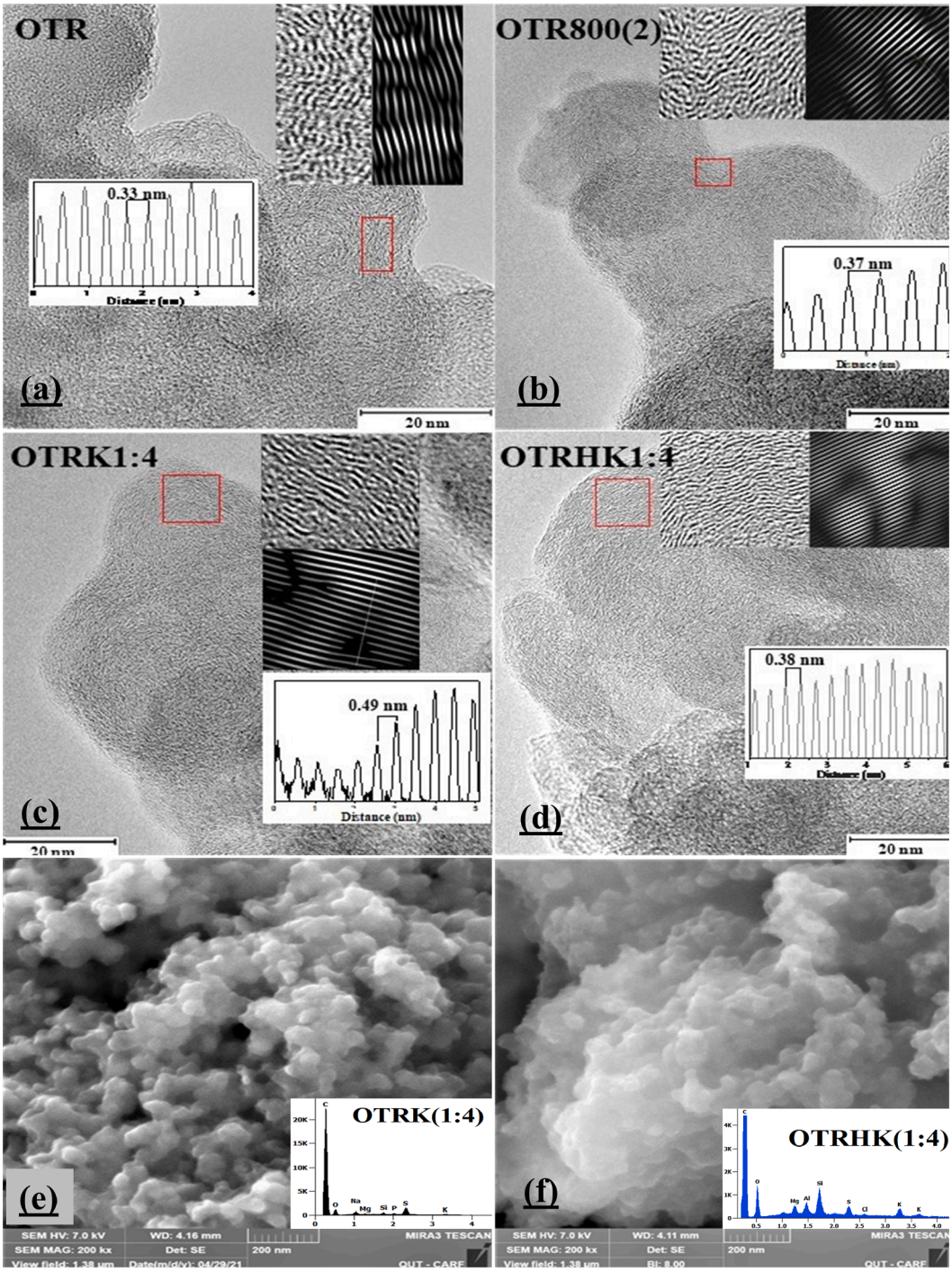

Fig. 2. HR-TEM image, FFT patterns, number of cycles, and interplanar distance of OTR (a), OTR800(2) (b), OTRK1:4 (c) and OTRHK1:4 (d); SEM-EDS of the two-step (e) and three-step approach (f), EDS acquired at 20 kV, Beam intensity:12, Working distance: 15 mm.

from K_2CO_3 after a series of redox reactions, converting to K_2O that reacts with hydrogen and carbon finishing in the exfoliation of potassium creating sites for gasification as described in Eqs. (5)–(8) (Al-Rahbi and Williams, 2016):

$$6KOH + 2C \rightarrow 2K + 2K_2CO_3 + 3H_2 \quad (5)$$

$$K_2CO_3 \rightarrow K_2O + CO_2 \quad (6)$$

$$K_2O + H_2 \rightarrow 2K + H_2O \quad (7)$$

$$K_2O + C \rightarrow 2K + CO \quad (8)$$

When ethanol was used for the impregnation of the alkali onto OTR (Table 2, entries 1 and 2) it was found to be less effective in increasing S_{BET} and porosity of the resulting carbon than the carbon obtained through mixing the alkali and OTR by grinding. It could be that the residual EtOH increases the volatilization process during carbonization and forms soot/carbon, which blocks the pores and channels in the carbon nanostructures. Among KOH treatments, using OTR:KOH ratio of 1:4 gives a comparable S_{BET} value independent of the processing method (Table 2, entries 4 and 6). As such, both processing methods show very similar nitrogen isotherms (Fig. 3(a)) and pore size distributions (Fig. 3 (b)).

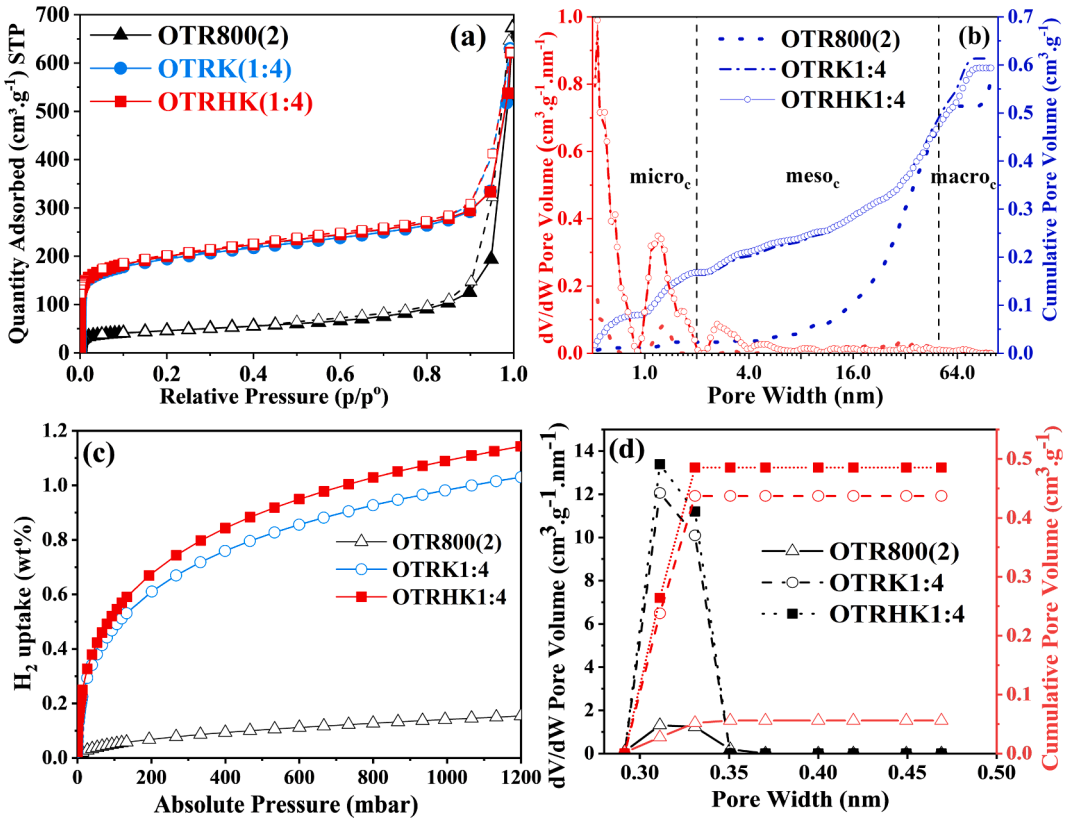

Fig. 3. N_2 (a) and H_2 (c) isotherm sorption at 77 K, pore size distribution of N_2 (b) and H_2 (d) absorbed of OTR800(2) and two and three-step approaches.

Table 2
Textural properties of OTR and carbonized OTR obtained by heating at 2 °C. min^{-1} to 800 °C and holding time of 1 h under nitrogen atmosphere.

Entry	Sample	S_{BET} ($m^2.g^{-1}$)	V_T ($cm^3.g^{-1}$)	$V\mu$ ($cm^3.g^{-1}$)	V_{meso} ($cm^3.g^{-1}$)	APS (nm)
1	OTRetK1:2	300.90	0.44	0.10	0.25	19.94
2	OTRNetK1:2	303.44	0.40	0.10	0.20	19.77
3	OTRK1:2	391.16	0.60	0.12	0.36	15.34
4	**OTRK1:4**	710.80	0.88	0.23	0.45	8.44
5	OTRHK1:2	596.28	0.64	0.22	0.28	10.06
6	**OTRHK1:4**	729.51	0.85	0.24	0.42	8.22
7	OTRN1:2	139.08	0.57	0.03	0.39	43.14
8	OTRKC1:2	273.83	0.95	0.06	0.63	21.91

With regard to the APS, the value decreased in the following order: OTR > NaOH 1:2 > K_2CO_3 1:2 > EtOH/KOH ~ EtOH/NaOH > KOH 1:2 > HCl/KOH 1:2 > KOH 1:4 > HCl/KOH 1:4, indicating that increasing the KOH ratio facilitates to separate the particles formed during carbonization. The APS value for OTRN1:2 was the highest (43.14 nm) as a result of when using NaOH instead of KOH under these conditions is not as effective to disrupt the aggregated structures of OTR (APS = 139 nm). The interaction between NaOH and carbon does not cause gasification (which aids particle disintegration) to the same extent as KOH (Lillo-Ródenas et al., 2003). The APS is an important parameter in the reinforcement industry, as smaller carbon particle sizes give better performance (Pilusa and Muzenda, 2013). Studies on NOx capture of waste tyre-derived carbons found that NOx capture increases with increasing S_{BET} and V_μ (Al-Rahbi and Williams, 2016), evidencing a possible application for these materials.

Raman spectra of the carbonized samples did not reveal any significant differences in the carbon graphitic structure and arrangement, implying that neither demineralization nor chemical treatment on their own or their combination affected the structural features of the carbonized materials. This is also confirmed by SEMs of these materials showing that surface morphologies of the materials produced by these two methods are not dissimilar as aggregate clusters of grape-like shapes, evident in both micrographs (Fig. 2(e), (f)).

Transmission electron microscopy (TEM) images show warm-like porous structures for all the samples, which to a certain extent confirm the pore size distribution data (Fig. 2(a), (b), (c), (d)). Fast Fourier transform (FFT) images and inverse fast Fourier transform images (IFFT) were used to determine the *d*-spacing of the lattice fringes of carbon structures.

A *d*-spacing of 0.33 nm, 0.37 nm, 0.38 nm, and 0.49 nm was found for OTR, OTR800(2), OTRHK1:4, and OTRK1:4, respectively. The *d*-spacing value indicates the degree of graphitization, and the smaller the value, the greater the degree of graphitization (Hu et al., 2004). Surprisingly, the *d*-spacing value of OTR800(2) did not undergo after demineralization or chemical treatment as it is very close to the graphite value of 0.3354 nm (Kim et al., 2014).

3.4. Surface functional properties

The high-resolution C1s spectra were deconvoluted into seven prominent peaks (Fig. A7) corresponding to C—C/C—H, C═C, C—N/C—O/C—S, C═O, COOH, CO_3 and pi → pi* bonds (Chen et al., 2020). Data from Table 3 shows that after carbonization, there were changes in the proportion of C—O and C═O functional groups. From O1s spectra, four prominent peaks were identified corresponding to ether and hydroxyl groups in aromatics (O—C(1), 533.4 eV), ether and hydroxyl groups bonded to aliphatics & carbonyl shake-up (O-C(2), 532.5 eV), carbonyl, lactone, and carboxylic groups (O═C, 531.2 eV) and absorbed oxygen or moisture (534.14 eV) (Fig. A8) (Smith et al., 2016). Lower peak values at 532.5 eV indicate a small presence of aliphatics groups and the possible presence of S and Si bonded to oxygen in not chemically

Table 3
The compositions of surface chemical functional groups related to high-resolution C1s and O1s by XPS.

		Assignment C 1s							Assignment O1s			
		Position (eV)							Position (eV)			
		284.8	285.5	286.5	288.5	289.6	289.8	291	533.4	532.5	531.2	534.1
Entry	Sample	C—C/C—H (at.%)	C═C (at.%)	C—O (at.%)	C═O (at.%)	COO (at.%)	CO_3 (at. %)	Pi—Pi*	O—C(1) (at %)	O—C(2), S—O, Si—O (at.%)	O═C, Zn—O (at.%)	O_2/H_2O (at.%)
1	OTR	75.30	11.90	4.80	2.60	2.50	0.80	2.00	67.10	3.70	12.90	16.30
2	OTR800(2)	65.20	12.40	7.40	4.60	3.30	1.30	5.90	64.10	6.60	5.90	23.40
3	OTRetK1:2	61.90	14.30	12.70	5.30	1.50	2.80	0.60	52.10	5.40	28.40	14.00
4	OTRNetK1:2	75.40	10.70	5.80	3.20	1.70	0.70	2.00	39.20	28.40	20.40	12.10
5	OTRK1:2	65.00	12.60	11.80	4.40	2.00	2.60	0.70	25.40	33.90	31.50	9.20
6	**OTRK1:4**	**60.00**	**11.00**	**11.40**	**5.00**	**2.10**	**1.50**	**9.00**	**7.50**	**29.90**	**60.20**	**2.30**
7	OTRN1:2	67.10	10.20	6.60	3.30	2.60	1.60	8.60	19.10	24.60	42.00	14.30
8	OTRHK1:2	65.40	13.20	9.30	4.10	2.70	2.30	2.70	53.00	22.30	19.90	4.90
9	**OTRHK1:4**	**63.70**	**14.70**	**7.80**	**3.90**	**3.00**	**1.90**	**5.10**	**21.80**	**21.00**	**55.30**	**2.00**
10	OTRKC1:2	71.10	10.60	7.20	3.20	2.50	0.80	3.50	44.80	29.60	10.70	15.00

treated residue and for the one-step wet impregnation of KOH (Table 3, entries 1, 2 and 3) (Yang et al., 2018). On the other hand, the peak related to ZnO at 531.15 eV overlapped with the O═C functional group (Guo et al., 2015); this could mean that this value can be more related to the formation of this metal oxide for untreated OTR. However, either the two-step or three-step methods substantially increased the carbonyl, lactone, and carboxylic groups. These features in the OTR-derived carbons suggest that they can be used as adsorbents or for catalysis applications.

3.5. Hydrogen storage as potential carbon structure application

Hydrogen will play a key role in the transition to a low carbon economy by replacing fossil fuels as a primary energy vector in transportation, manufacturing, and related industry sectors. The transformation to a future where H_2 plays these roles depends on its production, storage and delivery at competitive prices compared to natural gas and coal. The world can replace diesel, petrol and coal with clean energy based on the integration of H_2 with existing renewable energy generation technologies. Porous carbon materials are considered suitable storage and sorbent materials for H_2 due to their large surface area, pore structure, abundance, and low cost of production; they interact with H_2 in a non-covalent manner, thus providing an effective process for H_2 uptake and discharge (Mohan et al., 2019). Our carbons structures of OTR800(2) OTRHK1:4. OTRK1:4 were subsequently evaluated for H_2 sorption at a cryogenic temperature of 77 K (Fig. 3(c)). From the resulting isotherms, it can be seen an increase in H_2 uptake with increasing pressure. The carbon sample OTR800(2) which was obtained without demineralization and chemical treatment, shows a poor H_2 uptake. The S_{BET} of OTR800(2) is 4 times lower than the other two carbons and lower pore diameter, so the lower H_2 uptake recorded is not surprising.

The H_2 uptake for the other two carbons, OTRHK1:4 and OTRK1:4 increased sharply from 0 to 200 mbar before steadily rising to 1200 mbar, exhibiting the characteristic feature of monolayer adsorption of microporous materials (Sdanghi et al., 2020). From Fig. 3(c) the H_2 uptake of the carbon structure produced during the two-step approach, OTRK1:4 (1.03 wt%), is slightly lower than for the carbon produced by the three-step approach, OTRHK1:4 (1.14 wt%) because of its lower surface area S_{BET} (see Table 2). From Fig. 3(d), it is seen that apart from $S_{BET,}$ creating micropores with pore diameters up to 2 nm (Fig. 3(b)) from N_2 isotherms) is also critical for H_2 adsorption (Peng et al., 2020). Fig. 3(d)) clearly shows that the pore size distribution and pore diameter of the OTR carbon samples are in the range 0.30–0.35 nm where the uptake of H_2 occurs at these low pressures. These values are comparable with literature data for Ni-doped commercial activated carbon and plain graphene materials, where H_2 uptake is between 1.2 and 1.8 wt% under similar experimental conditions (Mohan et al., 2019).

XRD patterns (Fig. A5(a)) showed two broad diffraction peaks corresponding to (0 0 2) and (1 0 1) diffraction patterns of carbon materials, indicating the existence of partially nano graphitic arrangements usually observed for pyrolytic carbons. The empirical parameter R defined as the ratio of the height of the (0 0 2) peak (B) to the background (A), gives the approximate proportion of the number of parallel graphene sheets on the carbon surface (Qu, 2008, 2007). According to Qu (2007), when $R = 1$, the graphene layers are randomly distributed as single layers, and so the R-value is proportional to the amount of edge orientation on the carbon surface. The higher the R-value more elevated is the proportion of edge orientations (Qu, 2007). The R values in the two- and three-step approaches with KOH were higher than the untreated materials indicating a higher proportion of edge structures which confirms the presence of more active sites for H_2 adsorption for these carbons (Table A3). Deconvolution of the asymmetric 002 peak (Fig. A9) gives two peaks, the less-developed crystalline carbon (LDCC) and the more-developed crystalline carbon (MDCC). The LDCC value is highest in OTRHK1:4 associated with a higher number of aromatic layers with this structure, partly explaining why it has a higher H_2 uptake than OTRK1:4. So carbons with high S_{BET}, pore volume in the range < 2 nm, and high LDCC have higher H_2 uptake. From these results, to increase the H_2 uptake to higher values for carbonized OTR materials, methods to increase S_{BET}, micropore structure, higher proportion of edge structures could be obtained by replacing solid KOH with aqueous KOH, and changing the carbonization process should be also investigated.

3.6. Carbonized OTR as potential catalysts for biomass conversion

Due to their physical and thermochemical properties, carbon materials are gaining increasing interest in heterogeneous catalytic processes (Lázaro et al., 2015). Levulinic acid (LA) is considered a key chemical platform for fuels, polymers, pharmaceuticals, herbicides, and solvents. Aldol condensation of LA leads to products that have the potential as high-quality fuel precursors or chemical intermediates to produce liquid hydrocarbons (Hayes and Becer, 2020).

After eliminating non-reactive sulfur moieties such as metal sulfides and organic thiol groups during activation with KOH, OTRK1:4 was sulfonated with sulfuric acid (OTRK1:4-S) to increase the total acid sites to 1.96 $mmol.g^{-1}$ (Table A4). The amount of these acid sites in the material was determined using the titration method (Graber et al., 2017), and the sulfonated groups were also identified by XPS high-resolution S2p (Fig. A10) (Chhabra et al., 2019).

The sulfonated carbon was tested for LA Aldol condensation at 130 °C for 48 h (Table 4). The yields of LA condensation products, tetrahydro-2- methyl-5,γ-dioxo-2-furanpentanoic acid (TMDFA) and 3-(2-methyl-5-oxo- tetrahydrofuran-2-yl)-4-oxopentanoic acid (MOTOA) were calculated using ^1H NMR analysis. The product yields were calculated on the basis of the integration of the lactonic acid peaks over

Table 4
Free solvent levulinic acid conversion into lactone acid products.

Catalyst	Levulinic conversion (%)	TMDFA selectivity (%)	MOTOA selectivity (%)	Ref.
OTRK1:4-S, 6 h	1.00	0.30	0.51	This work
OTRK1:4-S, 48 h	64.47	21.71	74.14	This work
Commercial carbon-SO_3H, 6 h	20.00	15.00 (TMDFA + MOTOA)		(Amarasekara et al., 2019)
$ZnCl_2$ + trichloroaceticacid, 4.5 h	59.00	42.62	8.37	(Li et al., 2018)

Reaction conditions: levulinic acid (116 mg, 1.0 mmol) and solid acid catalysts (15 w/w%) were mixed in a small glass vial closed tightly and heated in an oil bath at 130 °C for 6 and 48 h. After the reaction, the resultant solution was diluted with t-butyl methyl ether (10 mL) and centrifuged at 1700 g for 10 min to separate the catalyst. The ether layer was concentrated and analysed using ^{1}H NMR spectra recorded in $CDCl_3$ using a Bruker spectrometer operating at 600 MHz; chemical shifts were given in ppm downfield from TMS ($\delta = 0.00$). For the quantification, DMSO was used as a standard.

LA singlet peak (Fig. A11).

In previous studies, it was revealed a yield of the LA dimers of 15% when using commercial sulfonated carbon as catalyst (Amarasekara et al., 2019), with a yield value of 59% found when a mixture of $ZnCl_2$ and trichloroacetic (50.9%) was used by Li et al., 2018 as catalyst during 6 h reaction time (Table 4). However, in our study with OTRK1:4-S, very low conversion of LA and dimers formation was achieved during the first few hours of reaction. Good yields of both TMDFA (21.7%) and MOTOA (74.1%) were only obtained after 48 h, suggesting slow reaction kinetics. The total acidity for the commercial sulfonated carbon is 1.1 mmol.g^{-1} (Amarasekara et al., 2019), lower than the value 1.96 mmol.g^{-1} obtained with OTRK1:4-S, and this difference does not explain the poor yield obtained with the latter catalyst at a short reaction time. It is likely that there are differences in the surface and adsorption properties between these catalysts that explain the time-dependency for the effectiveness of our catalyst. More studies are currently being conducted and will be the subject of another publication.

3.7. Inorganics recovery from the acid wash solution

Some of the minerals removed after the two-step approach activation of OTR were successfully recovered, as described in Fig. A1. Both a solid and a liquid phase were obtained at the end of the carbonization process. The liquid phase is predominantly ZnO (93.35% from the starting material) and K (42.36% from the starting material and added KOH) with minor amounts for Si (14.50% as SiO_2) and Fe (0.84% as Fe_2O_3). The metal Zn can be recovered by electrolysis from this phase and sold.

The acid wash obtained from the carbonized solid contains mainly K and Si with minor Zn and Fe salts. The neutralization process of the acid wash solution resulted in the recovery of 55.5% reactive SiO_2 (25.64% from OTR residue). The remaining Si (20.54% as SiO_2), Zn (1.71% as ZnO), and Fe (41.54% as Fe_2O_3) were recovered from the TBP phase (Fig. A12). The K recovered from the liquid phase and acid wash may be used in fertilizer formulations, and when sold would reduce processing costs. ^{29}Si MAS-NMR measurements were performed to assess the chemical SiO_2 networks of the Si recovered by the neutralization process. Four tetra-functional Si centres at −86.4, −93.8, −103.1, and −111.6 were labelled with the conventional Q_n notation where Q indicates to [(SiO)nSi(O$^{(-)}$)4 − n] units, n being the total of linking oxygen atoms surrounding the Si (Fig. 4a). The relative populations of Si conformational structures were estimated by deconvolution of the ^{29}Si NMR spectra into separate Gaussian peaks (Table A5) and shown in (Fig. 4c) (Jamiu and Ali, 2019; Rezende et al., 2018).

This finding complements the results derived from the FTIR, where the presence of silanol (3286.5 cm^{-1}), symmetric (v_s, 1058 cm^{-1}), and antisymmetric longitudinal and transversal optic modes of siloxane groups, SiO-SiO ($v_{as,}$ LO 1180 cm^{-1}, and TO 1052.7 cm^{-1}) (Warring et al., 2016) were identified in the recovered SiO_2 (Fig. 4b). Based on the

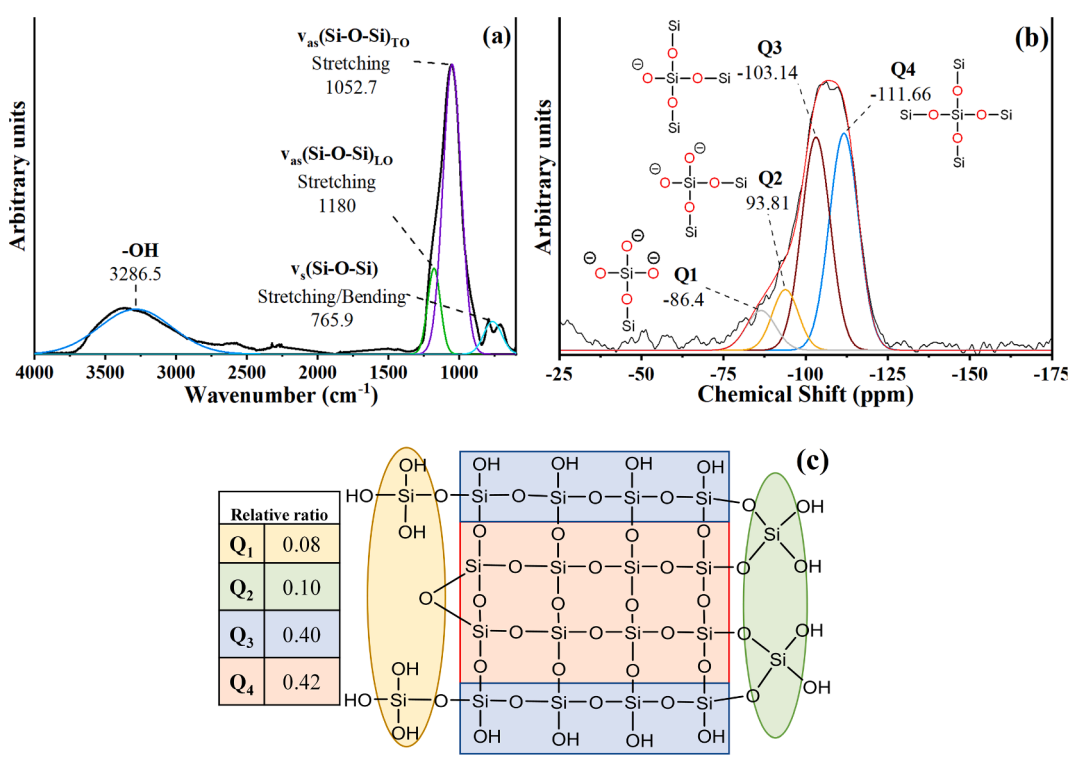

Fig. 4. FTIR-ATR (a) and ^{29}Si NMR (b) of SiO_2 from acid wash solution and projected structure of reactive silica recovered (c).

ratio between these groups' intensity, the recovered SiO_2's cross-linking ratio was estimated. The very high cross-linking ratio of 5.94 is remarkable compared to SiO_2 materials used for tyre manufacture. These SiO_2 materials are estimated to have a cross-linking ratio between 2.55 and 2.81 (Huabcharoen et al., 2017) and can only achieve these values with the aid of silane coupling agents.

This exceptionally high cross-linking ratio is explained by the condensation of silanol groups that arise during the carbonization of silica surfaces (Warring et al., 2016). As a result, a comparable relative ratio of Q_3 (0.40) and Q_4 (0.42) with a predominant presence of transversal symmetric Si-O-Si resonance and the possible formation of an organized double-layered Q_4-Q_3 structure where Q_4 SiO_4 is the main skeletal structure as suggested in Fig. 4c as reported by Jamiu and Ali, 2019.

From the SEM micrographs, the recovered SiO_2 showed a mixed morphology of the porous material (Fig. A13). This type of SiO_2 material is widely studied for applications such as in drug delivery (Kumeria et al., 2017), lithium-ion batteries (Entwistle et al., 2018), and the removal of toxic substances (Jamiu and Ali, 2019)

4. Conclusion

A two-step approach using KOH in the ratio 1:4 to OTR as the chemical activator was established to be found to be effective in the demineralization of OTR producing similar carbon structures with functional groups as achieved when using the conventional three-step approach process. Our study demonstrated that the demineralization step in the three-step approach used to remove the inorganics prior to the carbonization process is unnecessary as it increases the amount of wastewater to be processed and managed. In the present study, we have proven an effective way to manage the hazardous inorganic impurities and developed a simple process to recover ~ 55.5% of SiO_2 from the acid wash solution (25.64% from feedstock) with an exceptionally high cross-linking ratio with the potential to be used in many applications such as pharmaceutical, energy storage and tyre industries. We were also able to recover other inorganics, *e.g.* Zn (93.35%) from the carbonized residue, which could potentially be upgraded to pure metals. The carbon materials were tested for H_2 storage and were found to have comparable results as a commercial activated carbon evaluated for this purpose (1.03 wt% at 77 K and 1.2 bar). Also, the sulfonated carbon material showed promise as a catalyst for the Aldol condensation of levunilic acid to dimer products (64% conversion) which are precursors for fuels and chemicals. The current work has shown that OTR can be engineered to carbon materials with applications in important fields such as advanced materials, catalysis and energy storage.

Declaration of Competing Interest

The authors declare that they have no known competing financial interests or personal relationships that could have appeared to influence the work reported in this paper.

Acknowledgements

This project was supported by the Centre for Agriculture and the Bioeconomy (CAB), Queensland University of Technology, Queensland, Australia. The authors acknowledge the Central Analytical Research Facility (CARF-QUT) staff for assistance using the analytical equipment.

Appendix A. Supplementary material

Supplementary data to this article can be found online at https://doi.org/10.1016/j.wasman.2022.01.018.

References

Akyildiz, V., Özkan, A., Çokaygil, Z., Banar, M., Baydar, S., 2010. Improvement of solid product quality in pyrolysis of tyre derived fuels (TDF). Chem. Eng. Trans. 21, 775–780. https://doi.org/10.3303/CET1021130.

Al-Rahbi, A.S., Williams, P.T., 2016. Production of activated carbons from waste tyres for low temperature NOx control. Waste Manag. 49, 188–195. https://doi.org/10.1016/j.wasman.2016.01.030.

Amarasekara, A.S., Wiredu, B., Grady, T.L., Obregon, R.G., Margetić, D., 2019. Solid acid catalyzed aldol dimerization of levulinic acid for the preparation of C10 renewable fuel and chemical feedstocks. Catal. Commun. 124, 6–11. https://doi.org/10.1016/j.catcom.2019.02.022.

Antoniou, N., Zabaniotou, A., 2018. Re-designing a viable ELTs depolymerization in circular economy: Pyrolysis prototype demonstration at TRL 7, with energy optimization and carbonaceous materials production. J. Clean. Prod. 174, 74–86. https://doi.org/10.1016/j.jclepro.2017.10.319.

Australian Government, 2018. Report on the implementation of the Sustainable Development Goals: Report submitted to the high-level political forum on sustainable development. Creative Commons, Canberra.

Brunauer, S., Emmett, P.H., Teller, E., 1938. Adsorption of gases in multimolecular layers. J. Am. Chem. Soc. 60 (2), 309–319. https://doi.org/10.1021/ja01269a023.

Cardona, N., Campuzano, F., Betancur, M., Jaramillo, L., Martínez, J.D., 2018. Possibilities of carbon black recovery from waste tyre pyrolysis to be used as additive in rubber goods -a review-. IOP Conf. Ser. Mater. Sci. Eng. 437, 012012. https://doi.org/10.1088/1757-899X/437/1/012012.

Chen, W., Luo, M., Yang, K., Zhou, X., 2020. Microwave-assisted KOH activation from lignin into hierarchically porous carbon with super high specific surface area by utilizing the dual roles of inorganic salts: Microwave absorber and porogen. Microporous Mesoporous Mater. 300, 110178. https://doi.org/10.1016/j.micromeso.2020.110178.

Chhabra, T., Bahuguna, A., Dhankhar, S.S., Nagaraja, C.M., Krishnan, V., 2019. Sulfonated graphitic carbon nitride as a highly selective and efficient heterogeneous catalyst for the conversion of biomass-derived saccharides to 5-hydroxymethylfurfural in green solvents. Green Chem. 21 (21), 6012–6026.

Danmaliki, G.I., Saleh, T.A., 2017. Effects of bimetallic Ce/Fe nanoparticles on the desulfurization of thiophenes using activated carbon. Chem. Eng. J. 307, 914–927. https://doi.org/10.1016/j.cej.2016.08.143.

Danmaliki, G.I., Saleh, T.A., 2016. Influence of conversion parameters of waste tires to activated carbon on adsorption of dibenzothiophene from model fuels. J. Clean. Prod. 117, 50–55. https://doi.org/10.1016/j.jclepro.2016.01.026.

Entwistle, J., Rennie, A., Patwardhan, S., 2018. A review of magnesiothermic reduction of silica to porous silicon for lithium-ion battery applications and beyond. J. Mater. Chem. A 6 (38), 18344–18356.

Graber, E.R., Tsechansky, L., Fidel, R.B., Thompson, M.L., Laird, D.A., 2017. Determining acidic groups at biochar surfaces via the Boehm titration. Biochar A Guid. to Anal. Methods 85–94.

Guo, H.-L., Zhu, Q., Wu, X.-L., Jiang, Y.-F., Xie, X., Xu, A.-W., 2015. Oxygen deficient ZnO1-x nanosheets with high visible light photocatalytic activity. Nanoscale 7 (16), 7216–7223.

Gupta, R.K., Dubey, M., Kharel, P., Gu, Z., Fan, Q.H., 2015. Biochar activated by oxygen plasma for supercapacitors. J. Power Sources 274, 1300–1305. https://doi.org/10.1016/j.jpowsour.2014.10.169.

Hao, Y., Wang, Y., Wang, L., Ni, Z., Wang, Z., Wang, R., Koo, C.K., Shen, Z., Thong, J.T.L., 2010. Probing layer number and stacking order of few-layer graphene by Raman Spectroscopy. Small 6 (2), 195–200. https://doi.org/10.1002/smll.200901173.

Hayes, G.C., Becer, C.R., 2020. Levulinic acid: A sustainable platform chemical for novel polymer architectures. Polym. Chem. 11 (25), 4068–4077.

Henry, K.L., 2015. Upgrading pyrolytic tyre char through acid-alkali demineralisation. Stellenbosch University.

Hu, X.B., Cheng, G., Yun Zhao, B., Ming Wang, H., Hu, K.A., 2004. Catalytic effect of dopants on microstructure and performance of MCMB-derived carbon laminations. Carbon N. Y. 42 (2), 381–386. https://doi.org/10.1016/j.carbon.2003.11.010.

Huabcharoen, P., Wimolmala, E., Markpin, T., Sombatsompop, N., 2017. Purification and characterization of silica from sugarcane bagasse ash as a reinforcing filler in natural rubber composites. BioResources 12, 1228–1245. https://doi.org/10.15376/biores.12.1.1228-1245.

Iraola, I., Van Der Gryp, P., Görgens, J.F., 2018. A review on the demineralisation of pre- and post-pyrolysis biomass and tyre wastes. Waste Manag. 79, 667–688. https://doi.org/10.1016/j.wasman.2018.08.034.

Jamiu, Z.A., Ali, S.A., 2019. Construction of a double-layered polyelectrolyte-coated mesoporous silica containing residues of biogenic aspartic acid and its utilization for cadmium (II) removal. J. Sol-Gel Sci. Technol. 89 (3), 830–843. https://doi.org/10.1007/s10971-019-04920-9.

Kim, T.-H., Jeon, E.K., Ko, Y., Jang, B.Y., Kim, B.-S., Song, H.-K., 2014. Enlarging the d-spacing of graphite and polarizing its surface charge for driving lithium ions fast. J. Mater. Chem. A 2 (20), 7600–7605.

Kumeria, T., McInnes, S.J.P., Maher, S., Santos, A., 2017. Porous silicon for drug delivery applications and theranostics: recent advances, critical review and perspectives. Expert Opin. Drug Deliv. 14 (12), 1407–1422. https://doi.org/10.1080/17425247.2017.1317245.

Kupgan, G., Liyana-Arachchi, T.P., Colina, C.M., 2017. NLDFT Pore size distribution in amorphous microporous materials. Langmuir 33 (42), 11138–11145. https://doi.org/10.1021/acs.langmuir.7b01961.

Lázaro, M.J., Ascaso, S., Pérez-Rodríguez, S., Calderón, J.C., Gálvez, M.E., Jesús Nieto, M., Moliner, R., Boyano, A., Sebastián, D., Alegre, C., Calvillo, L., Celorrio, V.,

2015. Carbon-based catalysts: Synthesis and applications. Comptes Rendus Chim. 18 (11), 1229–1241. https://doi.org/10.1016/j.crci.2015.06.006.

Li, Z., Zhang, J., Nielsen, M.M., Wang, H., Chen, C., Xu, J., Wang, Y., Deng, T., Hou, X., 2018. Efficient C-C bond formation between two levulinic acid molecules to produce C10 compounds with the cooperation effect of Lewis and Brønsted acids. ACS Sustain. Chem. Eng. 6 (5), 5708–5711. https://doi.org/10.1021/acssuschemeng.7b04621.

Lillo-Ródenas, M.A., Cazorla-Amorós, D., Linares-Solano, A., 2003. Understanding chemical reactions between carbons and NaOH and KOH: An insight into the chemical activation mechanism. Carbon N. Y. 41 (2), 267–275. https://doi.org/10.1016/S0008-6223(02)00279-8.

Linares Solano, A., Lillo Ródenas, M.A., Marco Lozar, J.., Kunowsky, M., Romero Anaya, A., 2012. Utility of sodium and potassium hydroxides for preparing superior quality activated carbons. In: Calixto Carillo, A. (Eds.), Hydroxides: Synthesis, Types and Applications. Nova Science publishers, Inc., pp. 73–103.

Macías García, A., Díaz Díez, M.A., Alfaro Domínguez, M., Carrasco Amador, J.P., 2020. Influence of chemical composition, porosity and fractal dimension on the electrical conductivity of carbon blacks. Heliyon 6. https://doi.org/10.1016/j.heliyon.2020.e04024, 1 6.

Manocha, S., Prasad, G.R., Joshi, P., Zala, R.S., Gokhale, S.S., Manocha, L.M., 2013. Preparation and characterization of activated carbon from demineralized tyre char. In: AIP Conference Proceedings. American Institute of PhysicsAIP, pp. 109–112. https://doi.org/10.1063/1.4810039.

Martínez, J.D., Cardona-Uribe, N., Murillo, R., García, T., López, J.M., 2019. Carbon black recovery from waste tire pyrolysis by demineralization: Production and application in rubber compounding. Waste Manag. 85, 574–584. https://doi.org/10.1016/j.wasman.2019.01.016.

Meng, J., Li, S., Niu, J., 2019. Crystallite Structure Characteristics and Its Influence on Methane Adsorption for Different Rank Coals. ACS Omega 4 (24), 20762–20772. https://doi.org/10.1021/acsomega.9b03165.

Mohan, M., Kumar Sharma, V., Anil Kumar, E., Gayathri, V., 2019. Hydrogen storage in carbon materials. Energy Storage 1–26. https://doi.org/10.1002/est2.35.

Montes, V., Hill, J.M., 2018. Activated carbon production: Recycling KOH to minimize waste. Mater. Lett. 220, 238–240. https://doi.org/10.1016/j.matlet.2018.03.019.

Mwafy, E.A., 2020. Eco-friendly approach for the synthesis of MWCNTs from waste tires via chemical vapor deposition. Environ. Nanotechnol. Monit. Manag. 14, 100342. https://doi.org/10.1016/j.enmm.2020.100342.

Peng, Z., Xu, Y., Luo, W., Wang, C., Ma, L., 2020. Conversion of biomass wastes into activated carbons by chemical activation for hydrogen storage. ChemistrySelect 5 (36), 11221–11228. https://doi.org/10.1002/slct.202000877.

Phakam, B., Moghaddam, L., Baker, A.G., East, C., Doherty, W.O.S., 2017. Compositional and structural changes of sugarcane evaporator deposits after concentrated sodium hydroxide treatment. J. Food Eng. 214, 1–9. https://doi.org/10.1016/j.jfoodeng.2017.06.018.

Pilusa, J., Muzenda, E., 2013. Beneficiation of pyrolitic carbon black. Int. J. Chem. Nucl. Mater. Metall. Eng. 7, 392–396.

Qu, D., 2008. Investigation of hydrogen physisorption active sites on the surface of porous carbonaceous materials. Chemistry (Easton). 14 (3), 1040–1046. https://doi.org/10.1002/chem.200701042.

Qu, D., 2007. Investigation of oxygen reduction on activated carbon electrodes in alkaline solution. Carbon N. Y. 45 (6), 1296–1301. https://doi.org/10.1016/j.carbon.2007.01.013.

Randell, P., Baker, B., O'Farrell, K., 2020. Used tyres supply chain and fate analysis report. Castlemaine, Australia.

Rezende, C.A., Atta, B.W., Breitkreitz, M.C., Simister, R., Gomez, L.D., McQueen-Mason, S.J., 2018. Optimization of biomass pretreatments using fractional factorial experimental design. Biotechnol. Biofuels 11, 1–15. https://doi.org/10.1186/s13068-018-1200-2.

Saleh, T.A., Danmaliki, G.I., 2016. Influence of acidic and basic treatments of activated carbon derived from waste rubber tires on adsorptive desulfurization of thiophenes. J. Taiwan Inst. Chem. Eng. 60, 460–468. https://doi.org/10.1016/j.jtice.2015.11.008.

Sánchez-Olmos, L.A., Medina-Valtierra, J., Sathish-Kumar, K., Sánchez Cardenas, M., 2017. Sulfonated char from waste tire rubber used as strong acid catalyst for biodiesel production. Environ. Prog. Sustain. Energy 36 (2), 619–626. https://doi.org/10.1002/ep.12499.

Sdanghi, G., Canevesi, R.L.S., Celzard, A., Thommes, M., Fierro, V., 2020. Characterization of carbon materials for hydrogen storage and compression. J. carbon Res. 6, 1–28. https://doi.org/10.3390/c6030046.

Shah, J., Jan, M.R., Mabood, F., Shahid, M., 2006. Conversion of waste tyres into carbon black and their utilization as adsorbent. J. Chinese Chem. Soc. 53 (5), 1085–1089. https://doi.org/10.1002/jccs.200600144.

Sing, K.S.W., Williams, R.T., 2004. Physisorption hysteresis loops and the characterization of nanoporous materials. Adsorpt. Sci. Technol. 22 (10), 773–782. https://doi.org/10.1260/0263617053499032.

Smith, M., Scudiero, L., Espinal, J., McEwen, J.S., Garcia-Perez, M., 2016. Improving the deconvolution and interpretation of XPS spectra from chars by ab initio calculations. Carbon N. Y. 110, 155–171. https://doi.org/10.1016/j.carbon.2016.09.012.

Wang, H., Hu, H., Yang, Y., Liu, H., Tang, H., Xu, S., Li, A., Yao, H., 2020. Effect of high heating rates on products distribution and sulfur transformation during the pyrolysis of waste tires. Waste Manag. 118, 9–17. https://doi.org/10.1016/j.wasman.2020.08.015.

Wang, K., Xu, Y., Duan, P., Wang, F., Xu, Z.X., 2019. Thermo-chemical conversion of scrap tire waste to produce gasoline fuel. Waste Manag. 86, 1–12. https://doi.org/10.1016/j.wasman.2019.01.024.

Warring, S.L., Beattie, D.A., McQuillan, A.J., 2016. Surficial siloxane to silanol interconversion during room temperature hydration/dehydration of amorphous silica films observed by ATR-IR and TIR-Raman spectroscopy. Langmuir 32 (6), 1568–1576. https://doi.org/10.1021/acs.langmuir.5b04506.

Yang, H.W., Lee, D.I., Kang, N., Yoo, J.K., Myung, S.T., Kim, J., Kim, S.J., 2018. Highly enhancement of the SiOx nanocomposite through Ti-doping and carbon-coating for high-performance Li-ion battery. J. Power Sources 400, 613–620. https://doi.org/10.1016/j.jpowsour.2018.08.065.

Zhang, X., Li, H., Cao, Q., Jin, Li'e, Wang, F., 2018. Upgrading pyrolytic residue from waste tires to commercial carbon black. Waste Manag Res 36 (5), 436–444. https://doi.org/10.1177/0734242X18764292.